

Interlayer magnetoconductance of misoriented bilayer graphene ribbons

Sonia Ahsan,^{a)} K. M. Masum Habib, Mahesh R. Neupane, and Roger K. Lake^{b)}

Department of Electrical Engineering, University of California, Riverside, California 92521-0204, USA

(Received 12 September 2013; accepted 28 October 2013; published online 13 November 2013)

The coherent, interlayer conductance of misoriented bilayer graphene ribbons is a strong function of the Fermi energy and magnetic field. Edge states can result in a large peak in the interlayer transmission at the charge neutrality point that is several orders of magnitude larger than the surrounding low-energy transmission. The coherent interlayer conductance is consistently asymmetric around the charge neutrality point for all structures with the value differing by up to 3 orders of magnitude at $E_f = \pm 0.05$ eV. The low-energy states exhibit a high magnetoconductance ratio, and the magnetoconductance ratio tends to increase as the width of the ribbons decrease. The maximum value for the 35 nm wide bilayer ribbons at 10 T is 15 000%. Non-equilibrium Green's function calculations of the interlayer transport properties are also supported by semi-analytical calculations based on Fermi's Golden Rule. © 2013 AIP Publishing LLC. [<http://dx.doi.org/10.1063/1.4830019>]

I. INTRODUCTION

The electronic structure of bilayer graphene is highly sensitive to the stacking geometry.^{1,2} Experimentally, the layers of bilayer or multilayer graphene tend to be rotated (i.e., twisted or misoriented) with respect to each other.^{3–5} The need to understand the electronic properties of twisted graphene layers stimulated a number of theoretical and experimental investigations.^{4–16} The low energy states in each layer of misoriented bilayer graphene are effectively decoupled and maintain a linear dispersion for twist angles greater than a few degrees. Turbostratic graphitic structures maintain the high mobility of graphene.¹⁷ The electronic decoupling and high interlayer resistance is a coherent quantum effect resulting from destructive interference between the electron wavefunctions of the two rotated layers.⁸

The coherent interlayer transmission is a strong function of the twist angle, and it can be strongly suppressed giving high interlayer contact resistances.¹⁸ Bistritzer and MacDonald found coherent interlayer contact resistances changing by 16 orders of magnitude as the rotation angle is changed by 30°. Resistances values varied from $10^{15} \Omega\mu\text{m}^2$ to $0.1 \Omega\mu\text{m}^2$. Recent calculations of the phonon-mediated, interlayer conductance indicate that the phonon-mediated current is a significant interlayer transport mechanism at room temperature.¹⁹ The phonon-mediated current has a weaker dependence on rotation angle. At room temperature with a Fermi level 260 meV above the Dirac point, the interlayer resistance was found to smoothly vary from $50 \Omega\mu\text{m}^2$ at small rotation angles of a few degrees to $330 \Omega\mu\text{m}^2$ at a rotation angle of 30°. Experimental measurements found similar trends but a higher resistance that varied from $750 \Omega\mu\text{m}^2$ to $3400 \Omega\mu\text{m}^2$.²⁰

The coherent electronic decoupling between two dimensional rotated graphene sheets is still present when the overlap region is scaled to a few nanometers.⁹ Two armchair

nanoribbons (AGNRs) overlapping at an angle of 90° result in a misoriented overlap region with a crystallographic rotation angle of 30°. Even with an overlap region of $1.8 \text{ nm} \times 1.8 \text{ nm}$, the coherent interlayer transmission is reduced by approximately 5 orders of magnitude. In such structures, an interlayer voltage can result in a large modulation ($\sim 10^3$) of the coherent interlayer current.⁹ The vibrational modes and their effect on the current of the crossed graphene nanoribbon (GNR) system have not yet been investigated.

In addition to electronic properties, the unique chiral nature of quasi-particles in graphene results in a novel quantum Hall effect^{21–23} that opens a new possibility for spintronic applications.^{24,25} The integer quantum Hall effect in bilayer graphene indicates the presence of massive chiral quasiparticles²⁶ with a parabolic dispersion at low energy. The electron motion in twisted graphene is modulated by the application of an external perpendicular magnetic field (B-field). The B-field introduces the Peierls phase in the Bloch functions and thus modifies the energy-momentum dispersion, the subband spacings, the energy width, and the local density of states.^{27–29} At sufficiently large magnetic field, the cyclotron diameter of the electron motion becomes smaller than the GNR width, resulting in the formation of Landau levels.^{27,30}

GNRs can have interesting magneto-electronic properties with high magnetoresistance.^{24,31–33} GNRs with zigzag edges (ZGNRs) have shown magnetism both theoretically^{24,34,35} and experimentally.³⁶ A spin-valve device based on a graphene nanoribbon has been reported where the magnetoresistance is configured with two ferromagnetic (FM) states of ZGNR electrodes (parallel vs. antiparallel alignments), and the results of first-principles simulations exhibit high magnetoresistance values.²⁴ Saffarzadeh and Asl³³ investigated spin polarized transport of the planar FM/Graphene flake/FM junction with zigzag interfaces and showed that the junction exhibits a spin valve effect with magnetoresistance ratios as high as 95%. Experimentally a 10% magnetoresistance ratio in a GNR based spin valve

^{a)}Email: sahsan@ee.ucr.edu

^{b)}Email: rlake@ee.ucr.edu

device has been observed, where a 200 nm GNR was connected to NiFe contacts.³⁷ Another experimental study reported a negative magnetoresistance of nearly 100% at low temperatures, and over 50% at room temperature.³¹ Hwang and Sarma³⁸ predicted a negative magnetoresistance for intrinsic graphene and a nonmonotonic magnetoresistance for extrinsic graphene with a parallel magnetic field. In most of the previous studies, a magnetoresistance effect was induced by a change in the relative magnetic orientations of FM contacts.

In addition to the above intrinsic properties, novel van der Waals (vdW) heterostacks of graphene and non-graphene layers (MoS₂, hBN, Bi₂Te₃, TiO₂, etc.) have been demonstrated.^{39–50} Several types of heterostructures consisting of vdW materials have been proposed for various applications, such as high mobility electronic devices,³⁹ molecular scale electronic devices,⁴⁰ nonvolatile memory cells,⁴³ and magnetic field effect transistors.⁴⁴ The fabrication approach often consists of creating various individual materials by exfoliation and/or growth followed by mechanical stacking.⁴⁷ Such a procedure naturally leads to misoriented interfaces.

The coherent interplane transport between misoriented graphene layers is governed by quantum interference and the relative phases of the wavefunctions of the two layers. Since magnetic fields modify the phase of the electronic wavefunction, one might expect that the interlayer transport could be sensitive to an applied magnetic field. Any real structure is finite in size. It has edges where localized edge states can exist. If the scaling laws for heterostructure bipolar transistors serve as a guide, the horizontal dimensions of devices proposed to attain THz cutoff frequencies must be on the order of tens of nanometers.⁵¹ For these reasons, we investigate the interlayer transport between two stacked graphene ribbons with a crystallographic misorientation of 30°. Such a geometry results from an armchair ribbon on a zigzag ribbon. The widths of the nanoribbons considered range from 35 nm to 70 nm. The interlayer magnetoconductance (MC) is calculated as a function of Fermi level and perpendicular magnetic field. The magnetic field variation of the interlayer conductance can be large, changing by several orders of magnitude.

II. MODEL AND METHOD

A numerical approach and a semi-analytical approach are used to give insight into the interlayer coupling. The band structure calculations are performed using a tight binding π -bond model. The electron transmission and conductance are calculated using the non-equilibrium Green's function (NEGF) formalism. The interlayer transmission is also calculated semi-analytically using Fermi's golden rule and compared with NEGF results. The calculation methods and the device structure are discussed below.

A. Misoriented bilayer structures

Figures 1(a) and 1(b) show the schematic structure of the four-terminal misoriented bilayer graphene nanoribbon (mBGNR). It consists of two GNRs, an AGNR placed on top

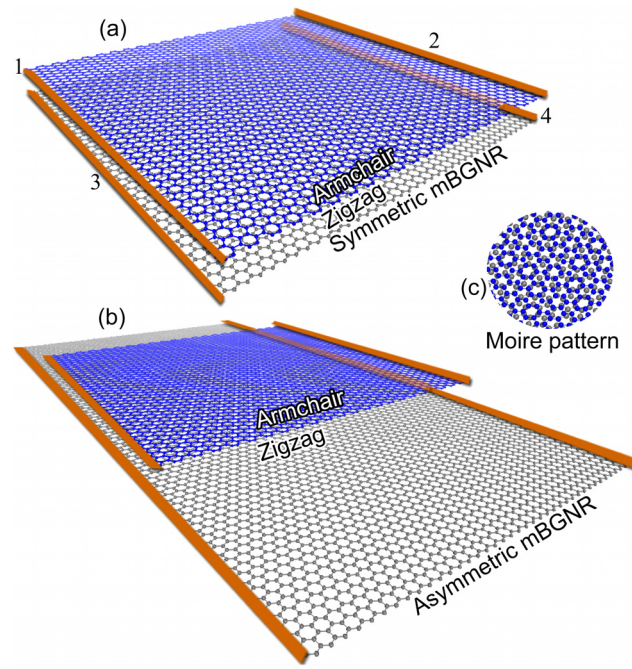


FIG. 1. mBGNR structures. In both structures, the top layer is armchair and the bottom layer is zigzag. Structure (a) will be referred to as the symmetric mBGNR since the dimensions of the top and bottom layers are identical. The 4 contacts to the structure are labeled. Structure (b) will be referred to as the asymmetric mBGNR, since the width of the armchair layer is less than that of the zigzag layer. For both structures, different widths are considered. The Moire pattern resulting from the overlap is shown in (c).

of a zigzag nanoribbon (ZGNR) with a vertical separation of 3.35 Å. The alignment of the two GNRs corresponds to a crystallographic misorientation angle of 30°. A 30° rotation is an incommensurate rotation angle,⁸ so that there is no periodicity in the bilayer structure. The top view of a section of the bilayer shown in Fig. 1(c) displays the Moire pattern resulting from the two misoriented graphene layers. Two types of mBGNRs are considered, symmetric structures in which both GNRs have the same width as shown in Fig. 1(a) and asymmetric structures in which the AGNR is narrower than the ZGNR as shown in Fig. 1(b). The asymmetric structures serve to move the overlap region away from the zigzag edges, which dominate the low-energy interlayer transmission.

The contact regions denoted by the gold termination at the ends of the nanoribbons are treated as semi-infinite continuations of the individual armchair or zigzag ribbon with no interlayer coupling. Physically, such a system would be implemented using a thin insulator such as BN with a window etched out. In the area of the window, the graphene layers would be in intimate contact. The contacts would be made outside of the window to the individual layers separated by the insulator.

B. Numerical model

The interlayer transport of the mBGNR is calculated using a tight-binding (TB) Hamiltonian with the NEGF formalism^{52,53} in the presence of an external perpendicular magnetic field. The intralayer nearest-neighbor hopping parameter is $\gamma_0 = 3.16$ eV. The interlayer hopping between

atom i on the top layer and atom j on the bottom layer is calculated using $\gamma_{ij} = \gamma_1 e^{-3(d_{ij}-d_0)}$, where d_{ij} is the distance between atom i and atom j , $\gamma_1 = 0.39$ eV is the interlayer nearest neighbor hopping, and $d_0 = 3.35$ Å is the inter-GNR distance.⁵⁴ The inplane cutoff distance is $3a_{cc}$, where a_{cc} is the C-C bond length. The applied perpendicular B-field of $\mathbf{B} = (0, 0, B_z)$ induces a vector potential $\mathbf{A} = (-B_z y, 0, 0)$. In the presence of an external perpendicular magnetic field, the coupling energy between neighboring atoms acquires a Peierls phase factor.⁵⁵ The coupling $\gamma_{0(1)}$ is modified to $\gamma_{0(1)} \exp(iq \int_m^{l_n} \mathbf{A} \cdot d\mathbf{l}/\hbar)$, where $l_{n(m)}$ is the coordinate of atom $n(m)$. The magnetic field is included in both the channel and the contact regions.

To compute the interlayer transmission $T(E)$ of such large aperiodic structures, the channel region is divided into $4a_{cc}$ wide blocks. Each block consists of a different number of atoms due to the non periodicity. The Hamiltonian matrix elements of these nonuniform blocks are used in a non-uniform recursive Green's function (RGF) algorithm to calculate the Green's function of the channel as described in Ref. 56. In the contact region, γ_1 is set to zero, so that the 4 contacts are isolated from each other. The self energies of the four contacts are calculated with the decimation method⁵⁷ using a 1 meV convergence factor. The transmission between a left contact on the top GNR and a right contact on the bottom GNR, $T(E)$, is calculated from the standard Green's function expression

$$T(E) = \text{tr}\{\Gamma_{1,1}^a G_{1,N}^R \Gamma_{N,N}^z (G_{1,N}^R)^\dagger\}, \quad (1)$$

where the indices 1 and N indicate the first and last block-layers of the mBGNR channel, respectively. Denoting the armchair contact self-energy on the left as $\Sigma_{1,1}^a$ and the zigzag contact self-energy on the right as $\Sigma_{N,N}^z$, then the injection matrices Γ in Eq. (1) are given by $\Gamma_{1,1}^a = i(\Sigma_{1,1}^a - \Sigma_{1,1}^{a\dagger})$ and $\Gamma_{N,N}^z = i(\Sigma_{N,N}^z - \Sigma_{N,N}^{z\dagger})$. The zero-temperature conductance G is given by

$$G = \frac{e^2}{h} T(E_F), \quad (2)$$

where E_F is the Fermi level. The MC ratio is

$$MC \equiv \frac{G(B) - G_0}{G_0}, \quad (3)$$

where $G(B)$ and G_0 are the conductance at a specific Fermi energy calculated at finite magnetic field and zero magnetic field, respectively. The diagonal elements of the spectral function, $A_{i,i}(E) = -2\text{Im}G_{i,i}^R(E)$, where i is the atom index, will be plotted to give insight into the spatial overlap of the wavefunctions on the two GNRs.

C. Analytical model

The analytical expression for $T(E)$ obtained from Fermi's golden rule is⁹

$$T(E) = 4\pi^2 \sum_{m,n} |M_{m,n}|^2 N_a^n(E) N_z^m(E). \quad (4)$$

The matrix element $M_{m,n}$ is calculated between a k_a state of mode n on the AGNR and a k_z state of mode m on the ZGNR. $N_a^n(E)$ and $N_z^m(E)$ are the 1D density of states of the armchair and zigzag nanoribbon, respectively. $T(E)$ depends on both the magnitude of the matrix element squared between the electron wavefunctions of the top and the bottom layers and the joint density of states of the two GNRs. The matrix element $M_{m,n}$ is calculated using the electronic wave functions of the isolated GNRs and expressed as

$$M_{m,n} \equiv \langle \psi_{m,k_z} | H_{\text{int}} | \psi_{n,k_a} \rangle, \quad (5)$$

where $|\psi_{m,k_a}\rangle$ and $|\psi_{n,k_z}\rangle$ are the Bloch wavefunctions for the armchair and the zigzag nanoribbons, respectively, and H_{int} is the interlayer component of the tight-binding Hamiltonian. The Bloch wavefunctions for the isolated armchair and zigzag nanoribbons are the eigenvectors of the tight-binding Hamiltonian H_k for each nanoribbon. The wavefunctions are extended over multiple unit cells of the nanoribbons using Bloch's theorem, $\psi_{m,k}(na) = e^{ikna} \psi_{m,k}(n=0)$, where a is the unit cell length along the nanoribbon, and n is the integer index of the unit cell.

III. RESULTS AND DISCUSSION

A. Magnetic field effect on the interlayer transport

Since the interlayer transmission can be calculated from the wavefunctions and density-of-states of the individual nanoribbons, it is useful to understand the effect of a magnetic field on the individual nanoribbons. First, consider the energy-momentum ($E - k$) dispersion relations resulting from the eigenvalues of H_k as a function of magnetic field. The band structures of the individual 35 nm wide AGNR and ZGNR are plotted at 4 values of perpendicular magnetic field as shown in Figs. 2(a)–2(h).

For the AGNR, at low magnetic field (0–2 T), the 2nd subband appears at ± 0.06 eV as shown in Figs. 2(a)–2(c). At higher magnetic fields (10 T), the subbands shift to higher energies as Landau levels begin to form.^{27,58,59} Also, as magnetic field increases (see Fig. 2(d)), the edge of the conduction band and the edge of the valence band flatten at the Dirac point.

For the ZGNR, the electronic band structure exhibits a flat band at the charge neutrality point even at $B = 0$ T due to the localized edge states.^{27,60} At low magnetic field (0–2 T), the 2nd subband appears at ± 0.09 eV. Like the AGNR, at higher magnetic fields, the subbands of ZGNR move further away.

The density of states of the individual nanoribbons that appear in Eq. (4) are proportional to the inverse velocity $\sim (\partial E / \partial k)^{-1}$. When the slope is flat, the density of states is large, and Eq. (4) indicates that this could result in peaks in the transmission. This is what will be observed in the NEGF calculations of transmission.

As the density of states of the armchair ribbon near the Dirac point increases with magnetic field, so also does the spatial overlap of the armchair and zigzag wavefunctions. Both wavefunctions become more localized near the edges of the nanoribbons. The spectral function $A_{i,i}(E)$ which is

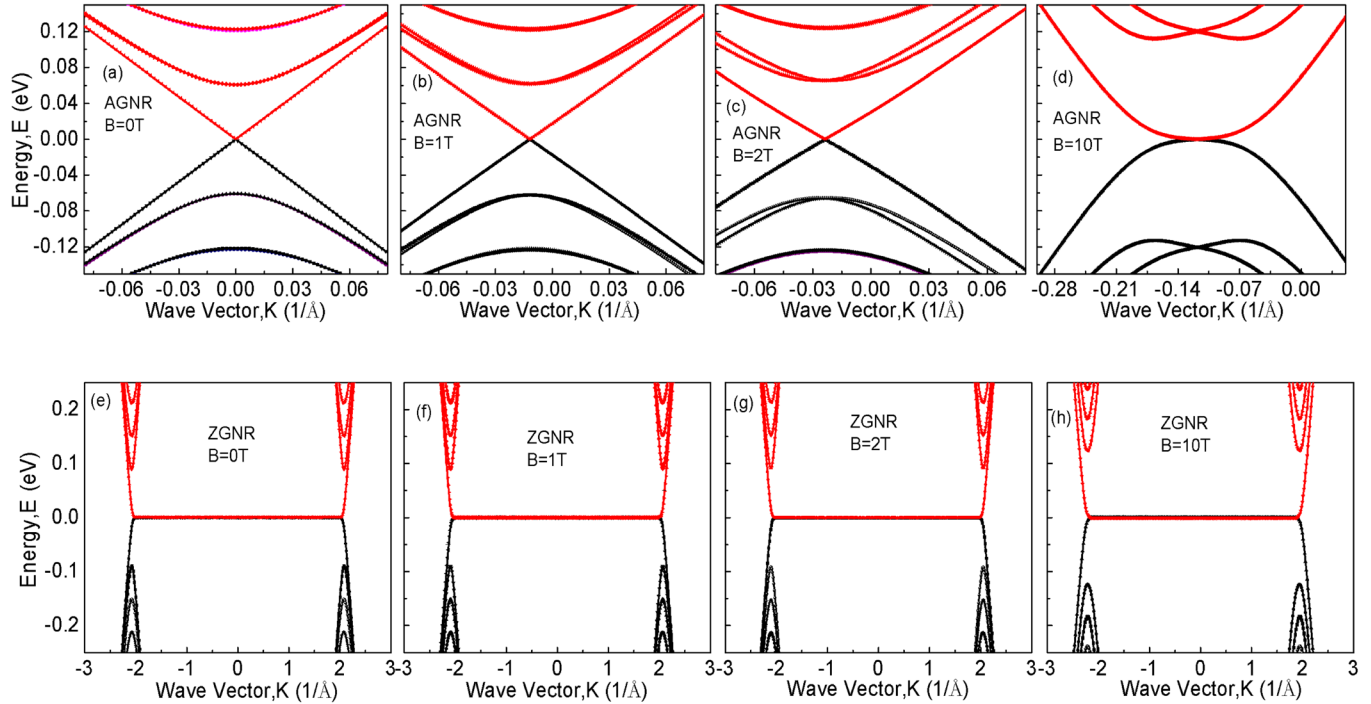


FIG. 2. Energy band structure of 35 nm individual single layer ((a)-(d)) AGNR and ((e)-(f)) ZGNR at $B = 0$ T, 1 T, 2 T, and 10 T, respectively.

proportional to the squared magnitude of the wavefunction on each atom in the unit cell consisting of 4 atomic layers is plotted as a function of its x -coordinate across the width of the nanoribbon in Fig. 3. Figs. 3(a) and 3(b) show the spatial distribution of the wavefunctions of the top (AGNR) and the bottom (ZGNR) layers of the 35 nm mBGNR, respectively, at magnetic fields of 0 T and 10 T near the charge neutrality point ($E = 0.05$ eV). At zero magnetic field, $|\psi|^2$ of the AGNR is distributed evenly across its width as shown in Fig. 3(a); whereas for the ZGNR, $|\psi|^2$ is more localized away from the center. At a magnetic field of 10 T, the magnitude of $|\psi|^2$ is maximum at the edges for both the AGNR and the ZGNR. The redistribution of the wavefunctions towards the edges of the GNRs and the flattening of the dispersion in Fig. 2(d) indicate that Landau levels and edge states are beginning to form. For wider GNR structures ($W = 50$ nm and 70 nm), the Landau levels form at lower magnetic fields since the Landau levels begin to form when the cyclotron diameter becomes smaller than the ribbon width.^{27,61}

The expression for the transmission in Eq. (4) depends on both the joint density of states and the matrix element squared. As the magnetic field increases, the wavefunctions of both the AGNR and the ZGNR have a higher weight at the edges of the nanoribbon increasing their spatial overlap. Also, as discussed above, the joint density of states near the Dirac point increases. Thus, both the wavefunction and the density of state dependence on the magnetic field suggest that the interlayer transmission should increase near the Dirac point as the magnetic field increases.

The interlayer transmissions $T(E)$ calculated from NEGF for the symmetric 35 nm, 50 nm, and 70 nm mBGNRs between contact 1 on the top GNR and contact 4 on the bottom GNR (as shown in Fig. 1(a)) are plotted in Figs. 4(a)–4(c) for increasing values of magnetic field. At $B = 0$ T, the magnitude of $T(E)$ is low throughout the energy window except near the charge neutrality point ($E = 0$). Near the charge neutrality point, the transmission peaks result from the edge states localized at the ZGNR edges. The low

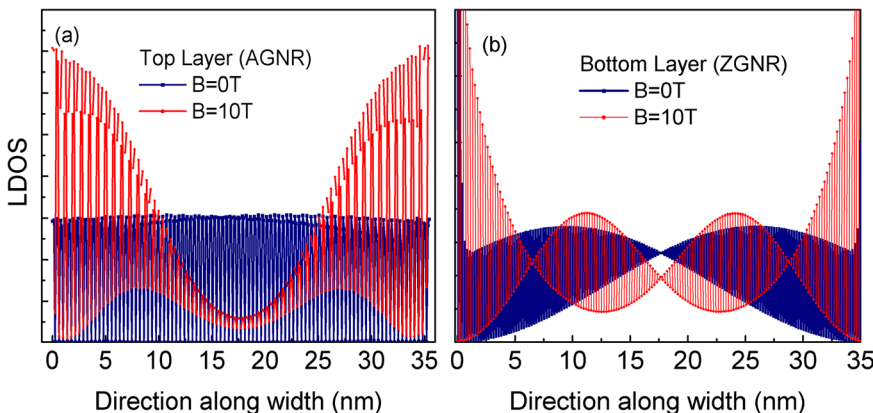


FIG. 3. Spectral function of (a) the top AGNR and (b) the bottom ZGNR for the symmetric 35 nm mBGNR structure at two different magnetic fields of 0 T and 10 T at $E_f = 0.05$ eV.

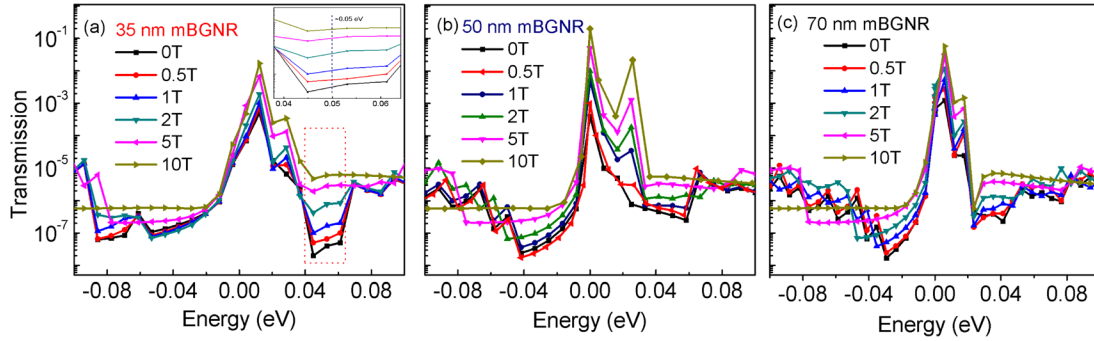


FIG. 4. Transmission spectrum for different magnetic fields of the symmetric (a) 35 nm (b) 50 nm, and (c) 70 nm mBGNR structures.

magnitude of $T(E)$ is consistent with the electronic decoupling found in recent experimental⁵ and theoretical studies⁸ of twisted bilayer graphene.

The coherent, interlayer conductance at zero magnetic field and temperature of the 50 nm mBGNR at Fermi energies of 0.05 eV and 0.225 eV are $\sim 1.9 \text{ S/cm}^2$ and $\sim 100 \text{ S/cm}^2$, respectively. At higher Fermi energies, the coherent conductance increases due to the presence of excited subbands. Bistritzer and MacDonald¹⁸ calculated an interlayer conductance between two infinite graphene sheets with a 30° misorientation angle and a Fermi energy of 0.26 eV of $\sim 0.4 \text{ S/cm}^2$. Their result depends sensitively on their value of the finite lifetime broadening which was 75 meV, so that a direct comparison of quantitative values is, perhaps, not too meaningful. It is, however, possible that the finite size increases the interlayer conductance due to the presence of the zigzag edge states at low energy and multiple modes at higher energies. An increase in the coherent interlayer conductance per unit area with decreasing width is consistent with other calculations of crossed armchair nanoribbons a few nanometers wide.⁹

The room-temperature, interlayer conductance between infinite graphene sheets with a 30° misorientation angle is mediated by a 30 meV beating-mode, interface phonon resulting in a phonon-mediated conductance of $\sim 3 \times 10^5 \text{ S/cm}^2$ at $E_F = 0.26 \text{ eV}$.¹⁹ This is 3 to 5 orders of magnitude larger than the coherent component of the conductance. Thus, low temperature and low bias are required to observe the coherent component of the conductance.¹⁹ At low bias such that only the phonon adsorption channel is available, the phonon-mediated current is proportional to the Bose-Einstein factor. Reducing the temperature from 300 K to 18 K reduces this factor by 10^8 , which would allow the coherent component of the conductance to dominate throughout the energy spectrum.

The transmission for all structures in Fig. 4 is asymmetric around the charge neutrality point. Since the density of states of the individual GNRs are symmetric around the charge neutrality point, the matrix element in Eq. (4) must be asymmetric. The asymmetry indicates that the coupling of the conduction bands is stronger than that of valence bands. Further analysis of the asymmetry using Fermi's golden rule will be discussed later. As the magnetic field is swept from 0 to 10 T, there can be several orders of magnitude change in the interlayer transmission (see inset of Fig. 4(a)).

The abrupt steps in transmission such as those of the 35 nm mBGNR at $\pm 0.06 \text{ eV}$ and $\pm 0.09 \text{ eV}$ result from the subbands in AGNR and ZGNR as previously discussed in Fig. 2. At the highest magnetic field of 10 T, the increasing energy of the Landau levels pushes the first step to higher energies outside the domain of the graphs. The qualitative trends in the transmission spectrum remain the same for the wider 50 nm and 70 nm structures shown in Figs. 4(b) and 4(c), respectively. The primary difference is that the transmission steps are more closely spaced since the subbands are closer in energy.

In the symmetric mBGNRs, the edge states of the ZGNR dominate the coherent transmission spectrum with peaks several orders of magnitude above the rest of the low-energy spectrum. To minimize the effect of the ZGNR edges, two different asymmetric mBGNR structures are considered where the ZGNR is wider than the AGNR. The two different structures consist of a 25 nm wide AGNR on a 50 nm wide ZGNR (50/25 mBGNR) and a 35 nm wide AGNR on a 70 nm wide ZGNR (70/35 mBGNR). Two qualitative trends in the transmission as a function of energy and magnetic field shown in Fig. 5 are similar to those of the symmetric mBGNRs. There is still large asymmetry between the electron and hole transmission. The change in the low-energy transmission with magnetic field is still large. There are also qualitative differences. The peak in transmission becomes narrower as the zigzag edges are moved away from the overlap region. This is expected since the edge states decay exponentially into the body of the ribbon. In the largest structure, the asymmetry around the charge neutrality point switches, such that the low-energy hole transmission is larger than the low-energy electron transmission. The line-shape of the transmission resembles that of a Fano resonance.⁶² Such a resonance results from a localized state weakly coupled to the continuum. In this case, there is the localized zigzag edge state weakly coupled to the continuum state of the armchair nanoribbon.

To demonstrate that the Fermi's golden rule expression of Eq. (4) captures the essential physics of the interlayer transmission, the transmissions of the 50/25 mBGNR structure calculated from Eqs. (4) and (1) are plotted in Fig. 6(a). The semi-analytical transmission from Eq. (4) captures the qualitative trends of the transmission including the large asymmetry between the electron and hole transmission and the peak near the charge neutrality point. The asymmetry results from the matrix element. This demonstrated by the

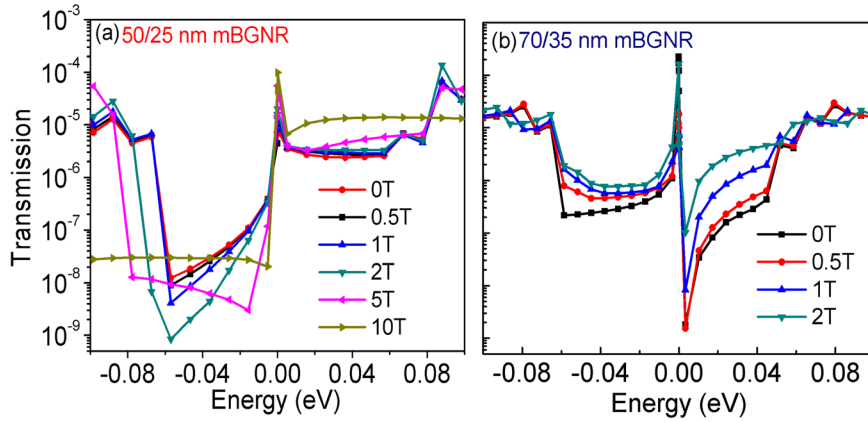


FIG. 5. Transmission spectrum for different magnetic fields of the asymmetric (a) 50/25 nm mBGNR and (b) 70/35 nm mBGNR structures.

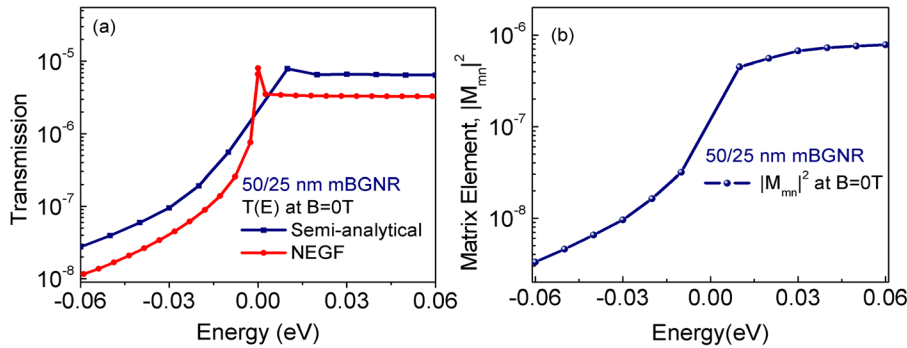


FIG. 6. (a) Comparison of the semi-analytical and the NEGF calculations of the transmission for the 50/25 nm mBGNR structure and (b) matrix element square of 50/25 nm mBGNR structure.

plot of the matrix element squared shown in Fig. 6(b). This asymmetric nature results from the interlayer interaction and stacking geometry. Lu *et al.*²⁹ studied the magneto-electronic properties of AA and ABC stacked graphite and found that the interlayer interactions destroy the symmetry about the Fermi level.

The coherent, interlayer magnetoconductance ratio as defined in Eq. (3) can be large. The zero-temperature, coherent magnetoconductance for 3 different structures with a Fermi energy of 0.05 eV is plotted versus magnetic field in Fig. 7. The narrowest 35 nm structure has the largest magnetoconductance ratio, and the magnetoconductance ratio tends to decrease with increasing width. For the 35 nm mBGNR heterostructure, the magnetoconductance ratio increased

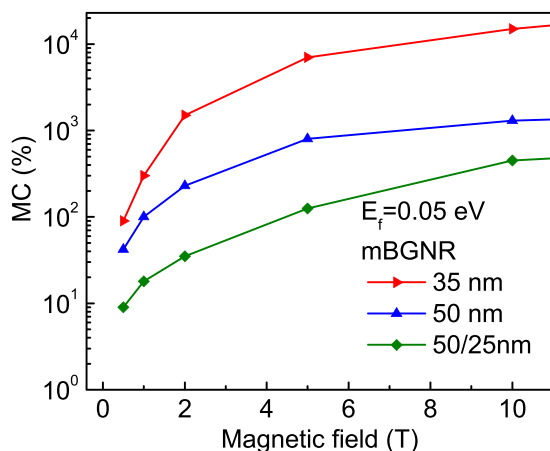


FIG. 7. Magnetoconductance ratios of different mBGNR structures at $E_f = 0.05$ eV.

from 90% at 2 T to 15 000% at 10 T. The maximum magnetoconductance ratio at 10 T of the 50 nm structure is 1300% and that of the 50/25 structure is 450%.

IV. CONCLUSIONS

The coherent, interlayer conductance of misoriented graphene nanoribbons is a strong function of energy and magnetic field. Experimental observation will require low temperature (< 20 K) and low bias (< 30 mV) to remove the phonon-mediated channel. When edge states are present in or near the overlap region, they result in a large peak in the coherent interlayer transmission at the charge neutrality point. The peak is several orders of magnitude larger than the surrounding low-energy transmission spectrum. The width of the peak is reduced as the edge states are moved away from the overlap region, since the edge states decay exponentially into the nanoribbon. The coherent interlayer conductance is consistently asymmetric around the charge neutrality point for all structures with the value differing by up to 3 orders of magnitude at $E_F = \pm 0.05$ eV. Since the density of states of the individual GNRs is symmetric, the asymmetry results from the matrix element of the wavefunctions. In the 70/35 structure in which the zigzag edge states have been moved the furthest from the overlap region, the asymmetry appears as a Fano resonance. This is consistent with the localized edge states being weakly coupled to the continuum states in the overlap region. The low-energy states exhibit a high magnetoconductance ratio, and the magnetoconductance ratio tends to increase as the width of the nanoribbons decrease. The maximum value at 10 T is 15 000%.

ACKNOWLEDGMENTS

This work was supported in part by FAME, one of six centers of STARnet, a Semiconductor Research Corporation program sponsored by MARCO and DARPA.

- ¹K. S. Novoselov, A. K. Geim, S. V. Morozov, D. Jiang, M. I. Katsnelson, I. V. Grigorieva, S. V. Dubonos, and A. A. Firsov, *Nature* **438**, 197 (2005).
- ²Y. Zhang, Y. W. Tan, H. L. Stormer, and P. Kim, *Nature* **438**, 201 (2005).
- ³J. Hass, R. Feng, J. E. Millan-Otoya, X. Li, M. Sprinkle, P. N. First, W. A. de Heer, E. H. Conrad, and C. Berger, *Phys. Rev. B* **75**, 214109 (2007).
- ⁴J. Hass, F. Varchon, J. E. M. Otoya, M. Sprinkle, N. Sharma, W. A. de Heer, C. Berger, P. N. First, L. Magaud, and E. H. Conrad, *Phys. Rev. Lett.* **100**, 125504 (2008).
- ⁵A. Luican, G. Li, A. Reina, J. Kong, R. R. Nair, K. S. Novoselov, A. K. Geim, and E. Y. Andrei, *Phys. Rev. Lett.* **106**, 126802 (2011).
- ⁶X. Wu, X. Li, Z. Song, C. Berger, and W. A. de Heer, *Phys. Rev. Lett.* **98**, 136801 (2007).
- ⁷S. Latil, V. Meunier, and L. Henrard, *Phys. Rev. B* **76**, 201402 (2007).
- ⁸S. Shallcross, S. Sharma, and O. A. Pankratov, *Phys. Rev. Lett.* **101**, 056803 (2008).
- ⁹K. M. M. Habib and R. K. Lake, *Phys. Rev. B* **86**, 045418 (2012).
- ¹⁰Z. Ni, Y. Wang, T. Yu, Y. You, and Z. Shen, *Phys. Rev. B* **77**, 235403 (2008).
- ¹¹R. Zhao, Y. Zhang, T. Gao, Y. Gao, N. Liu, L. Fu, and Z. Liu, *Nano Res.* **4**, 712 (2011).
- ¹²L. Xie, H. Wang, C. Jin, X. Wang, L. Jiao, K. Suenaga, and H. Dai, *J. Am. Chem. Soc.* **133**, 10394 (2011).
- ¹³J. M. B. Lopes dos Santos, N. M. R. Peres, and A. H. Castro Neto, *Phys. Rev. B* **86**, 155449 (2012).
- ¹⁴S. Shallcross, S. Sharma, E. Kandelaki, and O. Pankratov, *Phys. Rev. B* **81**, 165105 (2010).
- ¹⁵S. Shallcross, S. Sharma, and O. Pankratov, *Phys. Rev. B* **87**, 245403 (2013).
- ¹⁶D. Chae, D. Zhang, X. Huang, and K. V. Klitzing, *Nano Lett.* **12**, 3905 (2012).
- ¹⁷Y. R. Hernandez, S. Schweitzer, J.-S. Kim, A. K. Patra, J. Englert, I. Lieberwirth, A. Liscio, V. Palermo, X. Feng, A. Hirsch, M. Kläui, and K. Müllen, e-print [arXiv:1301.6087](https://arxiv.org/abs/1301.6087), 1 (2013).
- ¹⁸R. Bistritzer and A. H. MacDonald, *Phys. Rev. B* **81**, 245412 (2010).
- ¹⁹V. Perebeinos, J. Tersoff, and P. Avouris, *Phys. Rev. Lett.* **109**, 236604 (2012).
- ²⁰Y. Kim, H. Yun, S.-G. Nam, M. Son, D. S. Lee, D. C. Kim, S. Seo, H. C. Choi, H.-J. Lee, S. W. Lee, and J. S. Kim, *Phys. Rev. Lett.* **110**, 096602 (2013).
- ²¹V. P. Gusynin and S. G. Sharapov, *Phys. Rev. Lett.* **95**, 146801 (2005).
- ²²A. F. Morpurgo, *Nature (London)* **462**, 170 (2009).
- ²³C. Toke, P. E. Lammert, V. H. Crespi, and J. K. Jain, *Phys. Rev. B* **74**, 235417 (2006).
- ²⁴W. Y. Kim and K. S. Kim, *Nat. Nanotechnol.* **3**, 408 (2008).
- ²⁵F. M. Rojas, J. F. Rossier, and J. J. Palacios, *Phys. Rev. Lett.* **102**, 136810 (2009).
- ²⁶E. McCann and V. Fal'ko, *Phys. Rev. Lett.* **96**, 086805 (2006).
- ²⁷K. Wakabayashi, M. Fujita, H. Ajiki, and M. Sgrist, *Phys. Rev. B* **59**, 8271 (1999).
- ²⁸C. Chang, C. Lu, F. Shyu, R. Chen, Y. Huang, and M. Lin, *Physica E* **27**, 82 (2005).
- ²⁹C. L. Lu, C. P. Chang, and M. F. Lin, *Eur. Phys. J. B* **60**, 161 (2007).
- ³⁰G. Li and E. Y. Andrei, *Nat. Phys.* **3**, 623 (2007).
- ³¹J. Bai, R. Cheng, F. Xiu, L. Liao, M. Wang, A. Shailos, K. L. Wang, Y. Huang, and X. Duan, *Nat. Nanotechnol.* **5**(9), 655 (2010).
- ³²L. Brey and H. A. Fertig, *Phys. Rev. B* **76**, 205435 (2007).
- ³³A. Saffarzadeh and M. G. Asl, *Eur. Phys. J. B* **67**, 239–244 (2009).
- ³⁴Y. W. Son, M. L. Cohen, and S. G. Louie, *Nature (London)* **444**, 347–349 (2006).
- ³⁵Z. F. Wang and F. Liu, *Appl. Phys. Lett.* **99**, 042110 (2011).
- ³⁶C. Tao, L. Jiao, O. V. Yazyev, Y. Chen, J. Feng, X. Zhang, R. B. Capaz, J. M. Tour, A. Zettl, S. G. Louie, H. Dai, and M. F. Crommie, *Nat. Phys.* **7**, 616 (2011).
- ³⁷E. W. Hill, A. K. Geim, K. Novoselov, F. Schedin, and P. Black, *IEEE Trans. Magn.* **42**, 2694 (2006).
- ³⁸E. H. Hwang and S. D. Sarma, *Phys. Rev. B* **80**, 075417 (2009).
- ³⁹C. Dean, A. Young, L. Wang, I. Meric, G. Lee, K. Watanabe, T. Taniguchi, K. Shepard, P. Kim, and J. Hone, *Solid State Commun.* **152**(15), 1275–1282 (2012).
- ⁴⁰G. Eda, T. Fujita, H. Yamaguchi, D. Voiry, M. Chen, and M. Chhowalla, *ACS Nano* **6**(8), 7311–7317 (2012).
- ⁴¹K. S. Novoselov and A. H. C. Neto, *Phys. Scr., T* **146**, 014006 (2012).
- ⁴²B. Hunt, J. D. Sanchez-Yamagishi, A. F. Young, M. Yankowitz, B. J. LeRoy, K. Watanabe, T. Taniguchi, P. Moon, M. Koshino, P. Jarillo-Herrero, and R. C. Ashoori, *Science* **340**, 1427 (2013).
- ⁴³S. Bertolazzi, D. Krasnozhan, and A. Kis, *ACS Nano* **7**(4), 3246–3252 (2013).
- ⁴⁴S. B. Kumar, M. B. A. Jalil, and S. G. Tan, *Appl. Phys. Lett.* **101**, 183111 (2012).
- ⁴⁵H. Yang, J. Heo, S. Park, H. J. Song, D. H. Seo, K.-E. Byun, P. Kim, I. Yoo, H.-J. Chung, and K. Kim, *Science* **336**, 1140 (2012).
- ⁴⁶L. Britnell, R. V. Gorbachev, R. Jalil, B. D. Belle, F. Schedin, A. Mishchenko, T. Georgiou, M. I. Katsnelson, L. Eaves, S. V. Morozov, N. M. R. Peres, J. Leist, A. K. Geim, K. S. Novoselov, and L. A. Ponomarenko, *Science* **335**, 947 (2012).
- ⁴⁷A. K. Geim and I. V. Grigorieva, *Nature* **499**, 419 (2013).
- ⁴⁸S. Chuang, R. Kapadia, H. Fang, T. C. Chang, W.-C. Yen, Y.-L. Chueh, and A. Javey, *Appl. Phys. Lett.* **102**, 242101 (2013).
- ⁴⁹T. Georgiou, R. Jalil, B. D. Belle, L. Britnell, R. V. Gorbachev, S. V. Morozov, Y.-J. Kim, A. Gholinia, S. J. Haigh, O. Makarovskiy, L. Eaves, L. A. Ponomarenko, A. K. Geim, K. S. Novoselov, and A. Mishchenko, *Nat. Nanotechnol.* **8**, 100 (2012).
- ⁵⁰W. J. Yu, Z. Li, H. Zhou, Y. Chen, Y. Wang, Y. Huang, and X. Duan, *Nature Mater.* **12**, 246 (2013).
- ⁵¹M. J. W. Rodwell, M. Le, and B. Brar, *Proc. IEEE* **96**, 271 (2008).
- ⁵²S. Datta, *Electronic Transport in Mesoscopic System* (Cambridge University Press, Cambridge, 1995).
- ⁵³S. Datta, *Quantum Transport Atom to Transistor* (Cambridge University Press, Cambridge, 2005).
- ⁵⁴E. S. Morell, P. Vargas, L. Chico, and L. Brey, *Phys. Rev. B* **84**, 195421 (2011).
- ⁵⁵R. E. Peierls, *Z. Phys.* **80**, 763 (1933).
- ⁵⁶N. A. Bruque, M. K. Ashraf, T. R. Helander, G. J. O. Beran, and R. K. Lake, *Phys. Rev. B* **80**, 155455 (2009).
- ⁵⁷M. Galperin, S. Toledo, and A. Nitzan, *J. Chem. Phys.* **117**, 10817 (2002).
- ⁵⁸Y. C. Huang, C. P. Chang, and M. F. Lin, *Nanotechnology* **18**, 495401 (2007).
- ⁵⁹S. B. Kumar, M. B. A. Jalil, S. G. Tan, and G. Liang, *J. Appl. Phys.* **108**, 033709 (2010).
- ⁶⁰M. Fujita, K. Wakabayashi, K. Nakada, and K. Kusakabe, *J. Phys. Soc. Jpn.* **65**, 1920 (1996).
- ⁶¹S. B. Kumar, M. B. A. Jalil, S. G. Tan, and G. Liang, *J. Phys.: Condens. Matter* **22**, 375303 (2010).
- ⁶²U. Fano, *Phys. Rev.* **124**, 1866 (1961).